Modeling of laser beam absorption on rough surfaces, powder beds and sparse powder layers

Lupo, Giandomenico; Niemann, Martin; Goniva, Christoph; Szmyt, Wojciech; Jia, Xiao; Turlo, Vladyslav

DOI
10.1016/j.rinp.2024.108043

Publication date
2024

Document Version
Final published version

Published in
Results in Physics

Results in Physics 67 (2024) 108043

Contents lists available at ScienceDirect

Results in Physics

journal homepage: www.elsevier.com/locate/rinp

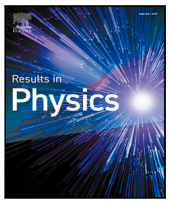

Modeling of laser beam absorption on rough surfaces, powder beds and sparse powder layers

Giandomenico Lupo [a,b], Martin Niemann [c], Christoph Goniva [c], Wojciech Szmyt [a], Xiao Jia [a], Vladyslav Turlo [a,*]

[a] Laboratory for Advanced Materials Processing, Empa-Swiss Federal Laboratories for Materials Science and Technology, Feuerwerkerstrasse 39, 3602, Thun, Switzerland

[b] Process and Energy Department, TU Delft, Leeghwaterstraat 39, 2628 CB, Delft, The Netherlands

[c] DCS Computing GmbH, Industriezeile 35, 4020, Linz, Austria

ARTICLE INFO

Keywords:
Laser
DEM
Rough surface
Powder bed
Ray tracing
Reflectivity

ABSTRACT

The energy transfer from a laser beam source to material surfaces with arbitrary geometrical features and variable surface roughness is the crucial step in many high-end engineering applications. We propose two models capable of predicting this energy transfer, applicable in different scenarios. The first is a high-fidelity numerical framework for the simulation of laser beam interaction with rough surfaces, which includes meshed geometry of arbitrary shape and material Lagrangian particles. The method discretizes the laser source as a collection of photon-type immaterial Lagrangian particles (Discrete Element Method) and is able to capture the effects of multiple reflections, angle-dependent reflectivity, and polarization change. Simulations were performed on a geometry reconstructed from a rough copper sample to reveal the impact of the polarization effects. This method is generally applicable to any surface where the effects of inelastic light scattering are not expected to play a significant role. The second model is a novel phenomenological correlation specifically designed to predict the effective reflectivity of sparse powder layers, which occur for example when metal vapor is recondensed and redeposited on the substrate during laser welding. The correlation is compared to the predictions obtained from the simulation framework and has been favorably compared to experimental data in a separate publication.

Introduction

The interaction of high-power laser beams with material surfaces is the fundamental physical phenomenon underlying numerous applications, ranging from welding and joining techniques to additive manufacturing and 3D printing, across automotive, aerospace, electronics, medical, and chemical industries. Many of these material modification applications involve complex coupled multi-physics phenomena at different scales, such as phase transition dynamics, convective and conductive heat fluxes, thermo-capillary driven flow, temperature-dependent material and transport properties, vapor plume dynamics, and optics [1]. Still, in all of them, the first and often controlling step is the energy input to the material from the laser source, upon which everything else is dependent. Direct measurements of the energy transfer from the laser beam to the material surface is often difficult or impractical [2]. Therefore a high-fidelity representation of the phenomenon is crucial for the predictive capabilities of any model of laser beam applications, and to advance their understanding, optimization, and operation. The accurate prediction of effective reflectivity is especially important in micro-welding and additive manufacturing, characterized by high energy density, with small time and length scales and large gradients in the system [3].

Most of the material surfaces used for practical purposes are characterized by a degree of roughness, which modifies their energy absorption/reflection properties compared with a polished sample of the same material. The simplest and most important mechanism to alter the energy transfer from a laser beam to a rough surface is the distribution of surface orientations encountered by the incident light rays, causing multiple reflections, self-shadowing, and non-uniform energy absorption [3–5]: depending on the surface morphology, part of the light source might even get trapped and be completely absorbed by the substrate, while shadowed pockets in the substrate might receive little to no energy. In practice, the global effective reflectivity of a rough surface is always lower than the nominal reflectivity value of the material, decreasing as the degree of roughness increases and approaching zero for a highly corrugated surface. Another more generally

* Corresponding author.
E-mail address: vladyslav.turlo@empa.ch (V. Turlo).

https://doi.org/10.1016/j.rinp.2024.108043
Received 16 May 2024; Received in revised form 16 October 2024; Accepted 11 November 2024
Available online 19 November 2024

relevant mechanism affecting the energy transfer is polarization. Many monochromatic laser beams used in applications are linearly polarized; the distribution of angles of incidence offered by the rough surface to the incoming light modifies its polarization state and enhances or reduces the energy transfer. There are also other phenomena influencing the energy transfer, such as temperature and state-of-matter dependence of the material reflectivity, and Raman scattering, but they are not considered in the present work. Furthermore, sophisticated periodic structures creating interference effects or material and wavelength-dependent specific plasmonic effects are also neglected.

Light reflection on uneven surfaces has been investigated with a variety of approaches. Some authors employ the classical treatment of the problem as a diffraction phenomenon induced by random surface features, causing phase scattering (Beckmann–Kirchhoff theory) [6]; numerical techniques for the scattering problem, as well as analytical solutions for special cases, are available [7]; they are however valid in the limit of perfectly conductive materials when no energy is transferred to the substrate, and usually single scattering without multiple reflections is considered [5]. These methods have therefore limited applicability to energy deposition problems and are more useful for the inverse problem of measuring the surface roughness from scattering/reflection data. An adaptive volumetric heat source has been used to represent heat penetration in powder beds due to multiple laser reflections [8], however, the replacement of a surface energy source with a bulk one inherently misrepresents the heat transfer dynamics and time scales, often leading to unrealistic results.

In this work, we contribute to the state-of-the-art of laser beam absorption modeling with a new simulation framework for the energy transfer from a laser beam source to a surface with arbitrary geometry, and with a novel correlation for the prediction of effective reflectivity of sparse powder layers. The mathematical and numerical features of the framework are described in Section "Discrete element method for laser beam absorption – Mathematical and numerical description". Section "Application to benchmark cases" presents the application of the model to two benchmark configurations, representative of common engineering applications. In the first case, the numerical method is applied to a stereophotogrammetry reconstruction of a rough copper sample. We demonstrate that the polarization effects included in the Fresnel reflection law are crucial for a realistic prediction of the energy transfer. In the second case, a powder bed is simulated, illustrating the interactions of photon-type particles with complex structures made of material particles and confirming that the energy transfer is consistent with the algebraic model for thick powder beds available in the literature. In Section "A correlation for the absorption of a laser beam by a sparse layer of powder particles", based on the powder bed simulation framework, we numerically investigate laser absorption on sparse powder layers, and develop a novel algebraic correlation for the effective reflectivity of such configurations, relating the geometric reflection factors of the powder layer to a sparseness parameter. We show that this correlation improves the reflectivity prediction compared to the one available for thicker powder beds. Finally, in Section "Conclusions" we summarize the findings of this work and trace some future developments for our numerical framework.

Discrete element method for laser beam absorption – mathematical and numerical description

A versatile high-fidelity method to numerically describe the interaction of a laser source with a material surface is the discretization of the laser beam into a finite number of rays, which are evolved by a ray tracing algorithm and suitable material interaction laws [4,9,10]. We present a novel ray-tracing-like framework for the interaction and energy transfer of a laser beam with material surfaces and Lagrangian particles, that models the laser as a collection of photon-type immaterial Lagrangian particles, inheriting the Discrete Element Method (DEM) from the commercial software Aspherix® [11]. Multiple specular reflections are handled by geometric optics, and energy transfer is implemented through Fresnel equations. The convenience of the framework lies in the unified DEM treatment of photon-type and standard-type particles, guaranteeing the easiness of implementation of a variety of configurations involving both meshed geometry and material particles at the same time. The photon-type particles benefit from the same efficient parallelization as standard-type DEM particles in Aspherix®, allowing for ample scale-up of computational cases in High-Performance Computing (HPC). Moreover, unlike most laser beam ray-tracing algorithms currently available [12,13], the treatment of photons with a separate Lagrangian-tracking algorithm allows the decoupling of the laser beam resolution from the system resolution (meshed geometry and Eulerian field domains), making the choice of the number of photons and their spatial distribution arbitrary and enabling finely tailored power inputs. The technical details of the method are provided below.

The laser beam is modeled as a discretized collection of individual photon-type particles, inheriting the DEM Lagrangian framework from the Aspherix® software. Mathematically, the photon-type particles are massless, frictionless, non-resolved Lagrangian particles, not subject to any forces, but possessing prescribed laws of interaction with material surfaces such as domain boundaries, meshes, and standard-type DEM particles. In practice, to fit into the general DEM framework of Aspherix®, photons are assigned a density and a radius; however, no momentum balance is applied to photon-type particles and these attributes are not used. Upon mutual contact (i.e. when occupying the same position at the same time) two photon-type particles pass through each other, without any interaction (this assumption is strictly valid only when no plasma initiation takes place [14]).

Nevertheless, the photon radius must be chosen sufficiently small with respect to the geometrical features of the simulation case, to ensure correct parallelization and interactions with such features. The present model assumes that the interaction of the laser with a material surface can be described fully with a single constant parameter, the optical reflectivity of the material being struck by the laser. This assumption holds for monochromatic laser beams, whose wavelength is much smaller than the geometric features of the surface so that reflection is purely specular and the energy spectrum remains unaltered. Thus, phenomena like diffraction, elastic and inelastic scattering, and diffuse reflection are excluded from the model. Nevertheless, as we will demonstrate in this work, the model provides a sufficiently accurate description of laser-metal interactions even if the laser wavelength is larger than the geometric features of the surface, especially when polarization effects are taken properly into account.

The model handles photon-type particles much in the same way as Aspherix® handles standard-type DEM particles: a set of material properties and interaction properties defines the particle features, while the insertion mode describes the injection of the particles into the computational domain. Photon-type particles are assigned the `laser` custom material and the `photon` material type; the interaction between photon-type objects and standard-type objects (boundaries, meshes, DEM particles) allows the choice of the reflection model (Schlick or Fresnel, see Section "Reflection coefficients") and of the energy threshold below which a photon is deleted from the computation. The `laser` insertion mode inherits from standard-type DEM particles the possibility to specify the shape and size of the inlet, the rate of insertion or number of inserted particles, and the time and duration of the insertion; additionally, for photon-type insertions, a custom-defined temporal and spatial energy distribution can be set.

Photons features

Each photon-type particle l has the following attributes:

- Position $\mathbf{x}_l$,

- Velocity $\mathbf{v}_l$,
- Energy E_l,
- Polarization $\mathbf{z}_l$,
- Reflection counter $N_{r,l}$.

In the absence of reflection events, the motion of the photon $\mathbf{x}_l(t)$ is described by the simple kinematic equation:

$$\frac{\mathrm{d}\mathbf{x}_l}{\mathrm{d}t} = \mathbf{v}_l, \tag{1}$$

while all the other photon attributes remain unchanged. Sections "Reflection coefficients"–"Calculation of reflections on spherical DEM particles" explain how such quantities are evolving upon occurrence of a reflection event.

The direction of the photon trajectory is given by $\mathbf{d}_l = \frac{\mathbf{v}_l}{|\mathbf{v}_l|}$. The unit vector that represents the polarization state, $\mathbf{z}_l$, is at all times orthogonal to the trajectory: $\mathbf{d}_l \cdot \mathbf{z}_l = 0$. The photon velocity magnitude, $|\mathbf{v}_l|$, is an arbitrary constant, equal for all photons, which is set as a simulation parameter and determines the choice of the time step Δt (see Section "Time integration"). A photon-type particle is deleted from the computation when its position falls out of the domain boundaries, or when its energy is lower than a chosen threshold, $E_l \leq E_{l,min}$.

Time integration

Eq. (1) is advanced by simple explicit Euler integration (Aspherix® uses a Verlet integration scheme for DEM particles, which is identical to explicit Euler when the particle velocity is constant):

$$\mathbf{x}_l^{n+1} = \mathbf{x}_l^n + \mathbf{v}_l^n \Delta t, \tag{2}$$

where the superscripts ^{n} and $^{n+1}$ denote quantities at time t_n and time $t_{n+1} = (t_n + \Delta t)$ respectively.

The choice of the time step Δt is prescribed by two considerations. Firstly, in order to detect all photon-geometry contacts, the distance traveled in one time step must not exceed the length scale Λ of the smallest geometrical feature of the system: $\Delta t \ll \frac{\Lambda}{|\mathbf{v}_l|}$. As previously mentioned, photon-type particles are assigned a fictitious radius, r_l, which must be itself much smaller than Λ to guarantee consistency in the treatment of communications between processes by the Aspherix® parallelization routines. The second consideration involves the skin size, i.e. the numerical parameter that defines the size of the region centered on each particle where checks for pairwise DEM interactions are performed by the algorithm. The detection of all particle–particle contacts (in the present case contacts between photon-type and standard-type particles) is ensured if the distance traveled by the photon in one time step does not exceed the skin size. Since it is customary, for computational efficiency, to choose a simulation skin size of the order of magnitude of the smallest particle radius, here $\mathcal{O}(r_l)$, and considering that $r_l \ll \Lambda$, it is the photon radius r_l, i.e. the smallest length scale in the simulation, that dictates the time step restriction:

$$\Delta t < \frac{r_l}{|\mathbf{v}_l|}. \tag{3}$$

Reflection coefficients

When a photon-type particle traversing an isotropic optical medium 1, with refractive index n_1, hits a wall boundary, a mesh cell or a standard-type DEM particle, made of an isotropic material 2 with refractive index n_2, a reflection event is triggered, which involves the calculation of the new photon trajectory, its new energy and polarization state.

Specular reflection is always assumed, and the optical properties of the system are described by the optical reflectivity of the interface between media 1 and 2, R:

$$R = \left(\frac{\phi - 1}{\phi + 1}\right)^2; \quad \phi = \frac{n_1}{n_2}, \tag{4}$$

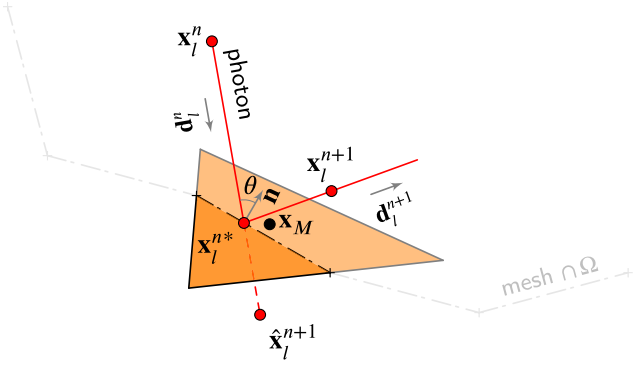

Fig. 1. Schematic depiction of a mesh reflection event. Aspherix® defines meshes by .stl files, therefore mesh elements are triangular. Note: distances in the picture are exaggerated for clarity; in reality, due to the time step restriction, the distance traveled in one time step $|\hat{\mathbf{x}}_l^{n+1} - \mathbf{x}_l^n| = |\mathbf{v}_l|\Delta t$ is (several times) smaller than the smallest mesh cell size.

The reflectivity R of a solid material with respect to light of a given wavelength is a common material property found in the literature; this value can be set in the model by choosing a pair of refractive indices such that $\phi = \frac{1-\sqrt{R}}{1+\sqrt{R}}$. Note that only the ratio ϕ of refractive indices enters the model. Furthermore, transmission is not accounted for: it is assumed that all light transmitted by material 2 is absorbed by it and converted into heat.

The exchange of energy with the material surface, depending on the angle of incidence θ, is based on one of two reflection models. The Fresnel model separates the reflectivity of $s-$ and $p-$polarized light [15]:

$$R_s = \left|\frac{\phi\cos\theta - \sqrt{1-(\phi\sin\theta)^2}}{\phi\cos\theta + \sqrt{1-(\phi\sin\theta)^2}}\right|^2; \quad R_p = \left|\frac{\phi\sqrt{1-(\phi\sin\theta)^2} - \cos\theta}{\phi\sqrt{1-(\phi\sin\theta)^2} + \cos\theta}\right|^2. \tag{5}$$

The Schlick model is independent of the polarization state [16]:

$$R_{Schlick} = R + (1-R)(1-\cos\theta)^5. \tag{6}$$

Calculation of mesh reflections

A material surface can be described by an analytical expression if its geometry is simple, or by a discretized mesh in all other instances. In the following, the reflection algorithm for the latter case is described. Extension to the case of a continuous geometry is straightforward.

The mesh resolution should be able to reproduce all the relevant geometrical features of the material surface, which in turn dictates a time step restriction for the time integration of Eq. (1), as the distance traveled by the photon-type particle in one time step must be smaller than the smallest mesh cell size in order to capture all mesh reflection events. This restriction is automatically satisfied when the stricter rule of Eq. (3) is applied, as discussed in Section "Time integration".

A mesh crossing event is detected when $(\hat{\mathbf{x}}_l^{n+1} - \mathbf{x}_M) \cdot \mathbf{n} \leq 0$, where $\hat{\mathbf{x}}_l^{n+1}$ is the photon position at time $t_{n+1} = (t_n + \Delta t)$, $\mathbf{x}_M$ is the position of the centroid of the closest mesh element, and $\mathbf{n}$ its normal unit vector. The plane of incidence Ω is identified by the unit vectors $\mathbf{n}$ and $\mathbf{d}_l^n$, the latter being the trajectory of the incident photon (see Fig. 1). The reflection point on the mesh element, $\mathbf{x}_l^{n*}$, is then calculated in the following manner:

$$|\hat{\mathbf{x}}_l^{n+1} - \mathbf{x}_l^{n*}| = \frac{(\hat{\mathbf{x}}_l^{n+1} - \mathbf{x}_M) \cdot \mathbf{n}}{\mathbf{d}_l^n \cdot \mathbf{n}}, \tag{7}$$

$$\mathbf{x}_l^{n*} = \hat{\mathbf{x}}_l^{n+1} - |\hat{\mathbf{x}}_l^{n+1} - \mathbf{x}_l^{n*}|\mathbf{d}_l^n. \tag{8}$$

The mesh crossing event becomes a reflection event, and the photon properties at time t_{n+1} are updated:

$$N_{r,l}^{n+1} = N_{r,l}^{n} + 1, \tag{9}$$

$$\mathbf{d}_l^{n+1} = \mathbf{d}_l^n - 2\left(\mathbf{d}_l^n \cdot \mathbf{n}\right)\mathbf{n}; \quad \mathbf{v}_l^{n+1} = \mathbf{d}_l^{n+1}|\mathbf{v}_l|, \tag{10}$$

$$\mathbf{x}_l^{n+1} = \mathbf{x}_l^{n*} + \mathbf{d}_l^{n+1}|\hat{\mathbf{x}}_l^{n+1} - \mathbf{x}_l^{n*}|. \tag{11}$$

To update the photon energy, E_l^{n+1}, first the angle of incidence θ is retrieved:

$$\cos\theta = -\mathbf{d}_l^n \cdot \mathbf{n}; \quad \sin\theta = |\mathbf{n} \times \mathbf{d}_l^n|, \tag{12}$$

whereby the reflection coefficients are calculated from Eq. (5) or Eq. (6), depending on the chosen reflection model. If Fresnel reflection is employed, then the polarization vector $\mathbf{z}_l^n$ at time t_n is decomposed into its $s-$ and $p-$components, respectively perpendicular and parallel to the plane of incidence Ω:

$$\mathbf{z}_l^n = \left(\mathbf{z}_l^n \cdot \mathbf{e}_s^n\right)\mathbf{e}_s^n + \left(\mathbf{z}_l^n \cdot \mathbf{e}_p^n\right)\mathbf{e}_p^n; \quad \text{with} \quad \mathbf{e}_s^n = \frac{\mathbf{n} \times \mathbf{d}_l^n}{|\mathbf{n} \times \mathbf{d}_l^n|}; \quad \mathbf{e}_p^n = \mathbf{d}_l^n \times \mathbf{e}_s^n, \tag{13}$$

which implies that the photon energy E_l^n at time t_n can also be decomposed into the fractions carried by the $s-$ and $p-$components of the electric field associated to the photon:

$$E_{l,s}^n = \left(\mathbf{z}_l^n \cdot \mathbf{e}_s^n\right)^2 E_l^n, \quad E_{l,p}^n = \left(\mathbf{z}_l^n \cdot \mathbf{e}_p^n\right)^2 E_l^n, \tag{14}$$

The updated total energy can then be reconstructed from the Fresnel coefficients:

$$E_l^{n+1} = R_s E_{l,s}^n + R_p E_{l,p}^n. \tag{15}$$

Likewise, the plane where the new polarization vector $\mathbf{z}_l^{n+1}$ lies, which is orthogonal to $\mathbf{d}_l^{n+1}$, is determined by the consideration that the $s-$component is unchanged, and the $p-$component is reflected within the plane of incidence Ω about the mesh normal $\mathbf{n}$, which gives:

$$\mathbf{e}_s^{n+1} = \mathbf{e}_s^n, \quad \mathbf{e}_p^{n+1} = \mathbf{e}_p^n + 2\left(\mathbf{d}_l^n \cdot \mathbf{n}\right)\left(\mathbf{e}_s^{n+1} \times \mathbf{n}\right). \tag{16}$$

Thus, the updated polarization vector $\mathbf{z}_l^{n+1}$ is given by:

$$\mathbf{z}_l^{n+1} = \sqrt{\frac{R_s E_{l,s}^n}{E_l^{n+1}}}\,\mathbf{e}_s^{n+1} + \sqrt{\frac{R_p E_{l,p}^n}{E_l^{n+1}}}\,\mathbf{e}_p^{n+1}. \tag{17}$$

If Schlick reflection is employed, the transfer of energy is polarization-independent and the photon energy after the reflection event is directly updated as:

$$E_l^{n+1} = R_{Schlick} E_l^n. \tag{18}$$

Finally, the temperature of the mesh element is raised by an amount ΔT that corresponds to the energy loss of the photon upon reflection:

$$\Delta T = \frac{E_l^n - E_l^{n+1}}{m c_p}, \tag{19}$$

where m and c_p are the mass associated with the mesh element and the heat capacity of the solid material respectively.

Supplementary Video 1 demonstrates the 2D case of photon particles in a hexagonal cage starting from the same initial positions and interacting with the walls following Fresnel law and Schlick approximation. The clear differences can be spotted immediately after the first few collisions in terms of energy loss and photon trajectories, with the Schlick approximation leading to faster photon removal according to the energy threshold.

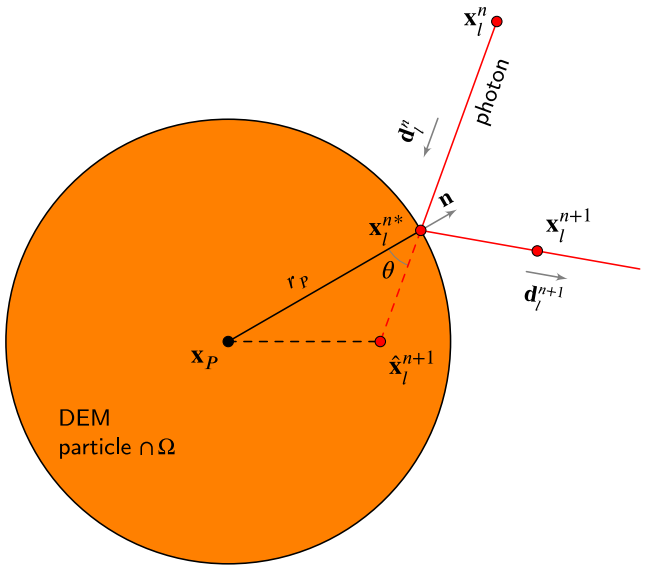

Fig. 2. Schematic depiction of a reflection event on a spherical standard-type DEM particle. Note: distances in the picture are exaggerated for clarity; in reality, due to the time step restriction, the distance traveled in one time step $|\hat{\mathbf{x}}_l^{n+1} - \mathbf{x}_l^n| = |\mathbf{v}_l|\Delta t$ is (several times) smaller than the particle radius r_P.

Calculation of reflections on spherical DEM particles

A collision event with a spherical standard-type DEM particle P is detected when $|\hat{\mathbf{x}}_l^{n+1} - \mathbf{x}_P| \le r_P$, where $\hat{\mathbf{x}}_l^{n+1}$ is the photon position at time $t_{n+1} = (t_n + \Delta t)$, $\mathbf{x}_P$ is the position of the particle centroid, and r_P is the particle radius. In this case, the plane of incidence Ω is identified by the vectors $(\hat{\mathbf{x}}_l^{n+1} - \mathbf{x}_P)$ and $\mathbf{d}_l^n$ (see Fig. 2). The reflection point on the particle surface, $\mathbf{x}_l^{n*}$, is then calculated in the following manner:

$$\mathbf{x}_l^{n*} = \mathbf{x}_l^n + \mathbf{d}_l^n\left(\left(\mathbf{x}_P - \mathbf{x}_l^n\right) \cdot \mathbf{d}_l^n - \sqrt{\left(\left(\mathbf{x}_P - \mathbf{x}_l^n\right) \cdot \mathbf{d}_l^n\right)^2 - \left(|\mathbf{x}_P - \mathbf{x}_l^n|^2 - r_P^2\right)}\right), \tag{20}$$

from which the normal to the reflection plane, $\mathbf{n}$, can be found:

$$\mathbf{n} = \frac{\mathbf{x}_l^{n*} - \mathbf{x}_P}{|\mathbf{x}_l^{n*} - \mathbf{x}_P|}. \tag{21}$$

The collision event becomes a reflection event, and the photon properties at time t_{n+1} are updated according to Eqs. (9)–(18).

Finally, the temperature of the standard-type DEM particle is raised by an amount ΔT_P that corresponds to the energy loss of the photon upon reflection:

$$\Delta T_P = \frac{E_l^n - E_l^{n+1}}{m_P c_p}, \tag{22}$$

where m_P and c_p are the mass of the standard-type DEM particle and the heat capacity of the solid material respectively.

As demonstrated in Supplementary Video 2, we also implemented the interactions of photons with other types of DEM particles accounting for more complex shapes than spherical ones. However, this implementation is outside of the scope of the current work and will be explored in detail in the follow-up works.

Application to benchmark cases

Two benchmark cases, indicative of typical laser processing applications, are selected to test the numerical model. In the first case, the energy absorption of a green laser beam on a copper plate with conspicuous surface roughness is numerically calculated. Increased effective absorptivity due to surface roughness is a frequent occurrence

in laser welding; we show that a model that correctly captures the effect of polarization on energy transfer is essential in obtaining a realistic prediction of the increased absorption. In the second case, the energy absorption properties of a powder bed made of mono-disperse spherical particles are investigated, through a parametric simulation study with varying optical reflectivity and powder bed thickness. Similar scenarios are encountered in laser powder bed fusion (LPBF), but also solar power receivers and other applications [17].

Laser absorption on a rough metallic surface

The reflectivity of a 25 × 10 × 2 mm polished copper plate, with purity of 99.9%, irradiated by a continuous wave Gaussian green laser beam (IPG, GLR-100) with 532 nm wavelength and beam waist radius ($1/e^2$) of 4.5 μ m, is measured at normal incidence as $R = (61.6 \pm 0.8)\,\%$, a value compatible with those reported in the literature [18,19]. The measuring apparatus consists of a power meter and a beam splitter, used to guide the reflected laser beam to the power meter, and is described in more detail in [20]. The reflected power from a silver-coated mirror, with known reflectivity, is used for calibration. The use of a short wavelength laser for copper microprocessing is justified by recent studies which show that the quality of microwelded parts in battery cells, electronics and automotive components can be significantly improved when green or blue laser beams are used instead of the more common infrared laser [21,22].

A microwelding test is subsequently performed on the same sample, whereby the surface roughness is altered in the vicinity of the welding track [20]. An increase in surface roughness is commonly observed close to welding regions, as a result of different phenomena induced by the laser scan, such as incomplete melting, liquid spattering, or deposition of nanoparticles from re-condensed metal vapors [20,23]. The roughness increase is expected to promote absorption and decrease the reflectivity with respect to the nominal value of the material. A relative reflectivity $\widetilde{R}$ can be defined as the ratio between the effective reflectivity of the rough surface and the original polished surface reflectivity:

$$\widetilde{R} = \frac{R_{\text{eff}}}{R}. \tag{23}$$

In order to convert the surface morphology into the simulation geometry, a patch of 2.3 × 1.5 μ m is scanned with an electron microscope (SEM).

Fig. 3 shows the method for digitizing the sample and discretizing it into a triangular mesh to be used in numerical simulations. First, two different SEM scans of the surface patch, at slightly different tilt angles, are acquired. These are processed in a stereophotogrammetry tool (the MountainsLab® software suite was used in the present case [24]), which reconstructs the 3D topography of the sample from the two 2D images. The output is a $(3 \times \Gamma)$ matrix of elevation data (z coordinate) and associated Cartesian grid coordinates (x and y), where Γ is the resolution of the scans in pixels (in the present case $\Gamma = 707\,584 = 1024 \times 691$ pixels). Table 1 shows the roughness statistics for the present copper sample, calculated from the reconstructed topography data. The geometry is then loaded into a 3D meshing tool (the free software MeshLab [25] was used) and converted into a mesh with the desired resolution and cell quality. A mesh of 17 430 triangles, with cell size of (25 ± 5) nm and aspect ratio of (0.6 ± 0.15) was generated for the present case, and saved to a `.stl` file.

Fig. 4 shows the simulation set up in four successive snapshots. The mesh is placed at the bottom of a box with periodic boundaries on the sides, and a photon exit boundary on top. At $t = 0$, N_l photons are initialized on a plane at $z_l^0 = 0.5 L_z$, with random and uniformly distributed horizontal coordinates $x_l^0 \in (0, L_x)$ and $y_l^0 \in (0, L_y)$. The photon velocity is initialized as $\mathbf{v}_l^0 = -|\mathbf{v}_l|\mathbf{e}_z$, while the polarization vector $\mathbf{z}_l^0$ lies in the $\mathbf{e}_x - \mathbf{e}_y$ plane. Table 2 summarizes the simulation parameters. The box height, L_z, is set at about three times the tallest peak of the mesh geometry, large enough that the photons have a sufficient reflection-free path before escaping from the top boundary, after each of them has reached its maximum number of mesh reflections. The simulation is advanced until all the photons leave the domain or exhaust their energy. Supplementary Video 3 shows the zoomed-in view of the photon interaction with the rough surface, highlighting one photon experiencing up to 5 reflections in the single well before escaping from it.

Table 1
Profile and area roughness statistics of the copper sample.

R_a [nm]	36.8	mean
R_q [nm]	47.1	rms
S_a [nm]	38.4	mean
S_q [nm]	51.5	rms

The effective reflectivity R_{eff} is calculated as the complementary value of the mesh absorptivity, defined as the total heat absorbed by the mesh divided by the initial energy of the photons. Thus it represents a measure of the hemispherical directional reflectance of the substrate. The relative reflectivity $\widetilde{R}$ is obtained from Eq. (23). Table 3 shows that a significantly different value of the reflectivity is obtained when the Fresnel reflection model is used as opposed to the Schlick reflection model, with the Schlick model leading to overprediction of the reflectivity, proving that the effect of polarization on the energy transfer cannot be neglected when R is large enough. It follows from Eq. (5) that the relative weight of the absorption of p−polarized light for θ close to Brewster's angle θ_B (defined as $R_p(\theta_B) = \min\{R_p(\theta)\}$ [15]) becomes increasingly significant as R grows larger. This is illustrated in Fig. 5, where Eqs. (5) and (6) are compared for the reflectivity value of the polished copper surface, $R = 0.616$. Assuming that the reflection points on the irradiated surface are randomly oriented, so that the contributions of s− and p−polarized light are equal over all angles of incidence, the average of the R_s and R_p coefficients, $(R_s + R_p)/2$, can be compared to $R_{Schlick}$: for $R = 0.616$ the two (solid-line) curves are considerably different, justifying the increase in total absorptivity observed when polarization effects are included in the simulation. The inset of Fig. 5 shows that, for a small value of the optical reflectivity ($R = 0.1$ in the plot), the effect of polarization on the total energy transfer is negligible, and the Schlick model becomes a reasonable approximation.

It is to be noted that the laser wavelength (532 nm) used in the experiment is about one order of magnitude larger than the mean and root mean square surface roughness of the sample (Table 2): this implies that effects of scattering (both elastic and inelastic) cannot in principle be neglected, and the use of a model based on geometric optics is not necessarily appropriate. Therefore, the simulation result here must be strictly interpreted as a verification that the numerical model correctly predicts the energy exchange based on its assumptions, rather than an attempt to validate the model with experimental data. On the other hand, the reflectivity value for the rough copper sample (reported in "Appendix A"), measured at normal incidence with the same apparatus used to characterize the polished sample and described in detail in [20], comes very close to the value predicted by the simulation. This might indicate that specular reflection at a fixed wavelength, purely governed by geometric optics, is the predominant mechanism of heat transfer for the present system, but the limitedness of our experimental data does not allow to draw a definitive conclusion to support this claim, and the comparison between the two values is to be considered qualitative. A more extensive experimental campaign across samples of different roughness, carried out with an integrating sphere apparatus to capture diffuse reflection, would provide more decisive insight about the range of applicability of the numerical model and the mechanisms of energy transfer, but is beyond the scope of the present work.

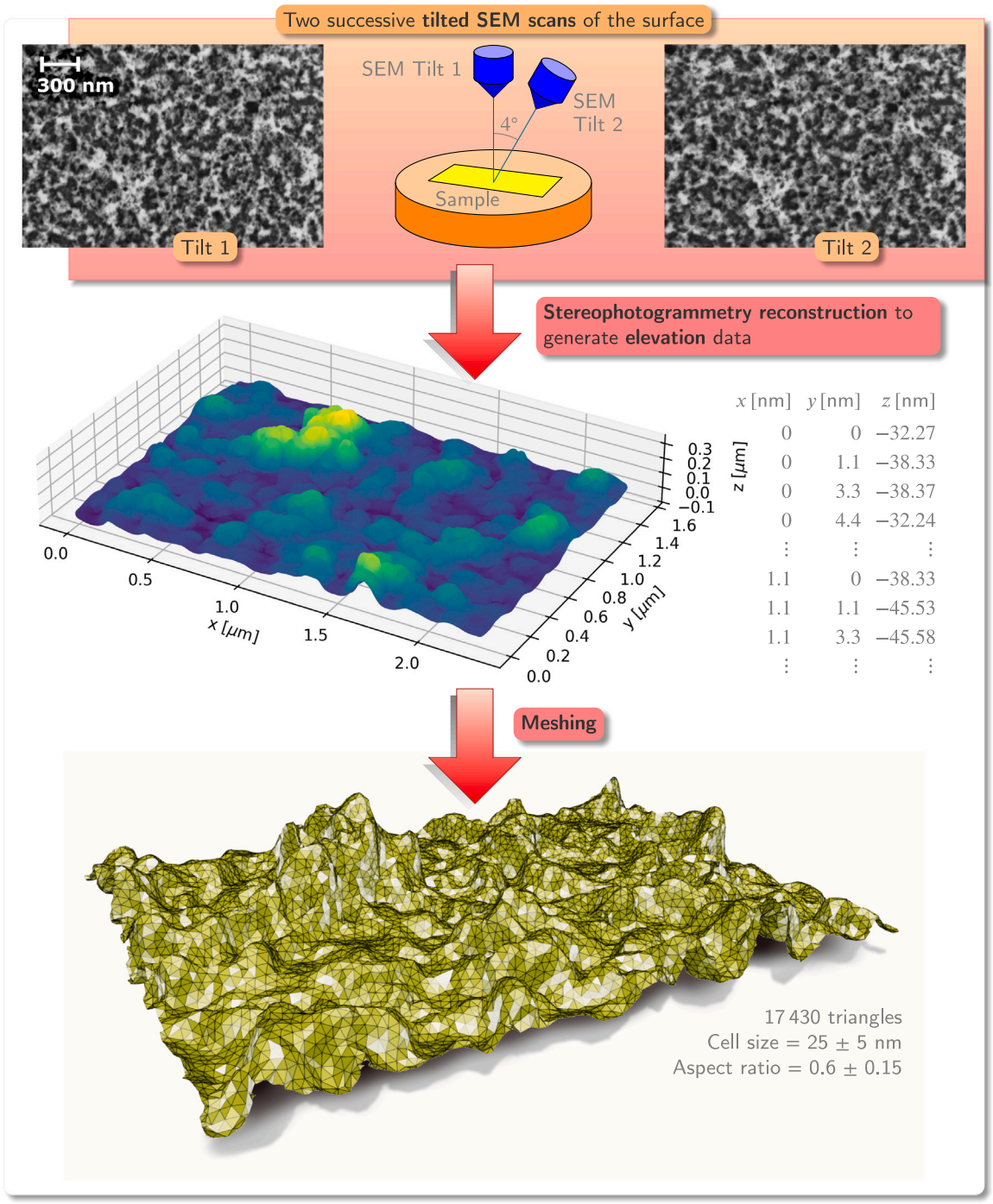

Fig. 3. 3D mesh generation procedure from 2D SEM scans of a metallic surface.

Laser absorption on a thick powder bed

Powders are usually poly-disperse and exhibit a variety of shapes, characteristics which variably affect the reflection and scattering behavior of a powder bed. Investigation of these factors is however left to future work. The simplest representation of a powder bed, which is employed hereafter, is a mono-disperse layer of spherical standard-type DEM particles on a flat substrate. The substrate is placed at the bottom of a cubic box with periodic boundaries on the sides. Prior to the laser simulation, the DEM powder particles are uniformly initialized in a region at the top of the box and let freely fall onto the substrate by gravity, with no cohesion force between them. This pre-simulation stage is completed when all the powder particles have come to their final settling position, i.e. when the maximum particle velocity is below 1×10^{-12} m/s (that is 10^{-10} of their peak velocity when hitting the substrate). Supplementary Video 4 shows the powder settling process for a sparse powder bed with near monolayer thickness. After the powder bed is settled, it is then hit by $N_l = 50\,000$ photon-type particles, interacting with the powder bed and exiting from the boundary on top (see Supplementary Video 5).

Fig. 6 shows two successive snapshots of the simulation setup for a thick powder bed, in which $N_P = 14\,324$ powder particles are arranged in irregular loose packing on a flat substrate made of the same material, forming a bed around 6.5 powder particle diameters thick, with a measured packing density (solid volume fraction) of $\epsilon_d = 0.573$, which is around the lower limit of solid volume fractions for irregular packing

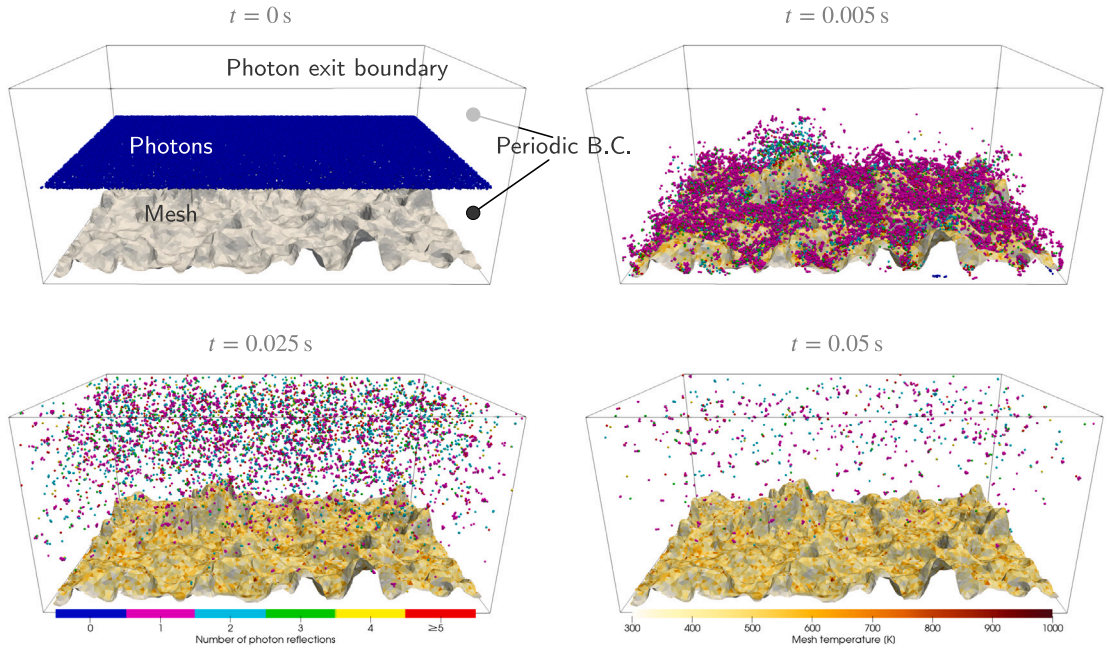

Fig. 4. Simulation set up of the rough copper plate in four successive snapshots. The mesh is colored by its temperature, the photon-type particles are colored by the number of reflection events $N_{r,l}$. (For interpretation of the references to color in this figure legend, the reader is referred to the web version of this article.)

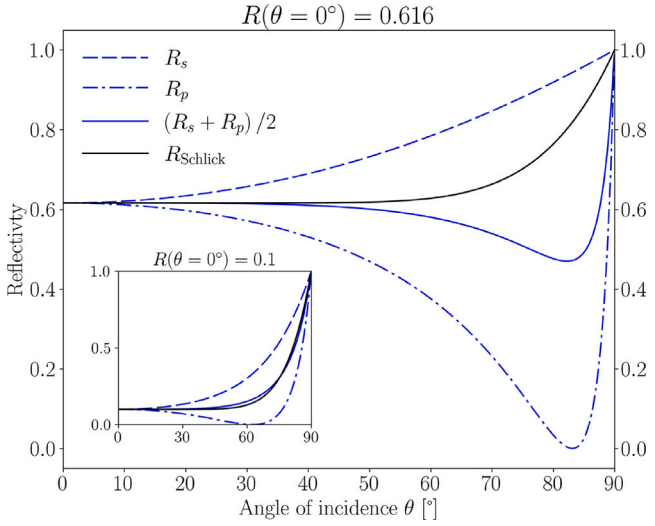

Fig. 5. Reflectivity according to the Fresnel and Schlick reflection models, as a function of the angle of incidence θ, for an optical reflectivity at normal incidence $R(\theta = 0°) = 61.6\%$. The inset shows the comparison between the Fresnel and Schlick models for $R(\theta = 0°) = 10\%$.

Table 2
Simulation parameters for the copper plate case.

$L_x \times L_y \times L_z$	Box size [μm]	2.35 ×1.55× 1.00
N_l	Number of photons	50 000
E_l^0	Photon energy [kJ]	8
$E_{l,min}$	Photon energy threshold [kJ]	1×10^{-12}
r_l	Photon radius [nm]	1
$\lvert\mathbf{v}_l\rvert$	Photon velocity magnitude [m/s]	1×10^{-6}
Δt	Time step [s]	5×10^{-7}
R	Reflectivity of the mesh material	0.616
Λ	Mesh cell size [nm]	25 ± 5
c_p	Mesh heat capacity [J/kg K]	481
ρ	Mesh density [kg/m^3]	7990
δ_A	Mesh thickness [nm]	0.1

Table 3
$\widetilde{R}$ calculated from the simulation.

Simulation (Fresnel)	54.4%
Simulation (Schlick)	69.3%

Table 4
Simulation parameters for powder bed cases.

$L_x \times L_y \times L_z$	Box size [mm]	10 × 10 × 10
N_l	Number of photons	50 000
E_l^0	Photon energy [kJ]	8
$E_{l,min}$	Photon energy threshold [kJ]	1×10^{-12}
r_l	Photon radius [nm]	10
r_P	Powder particle radius [μm]	100
$\lvert\mathbf{v}_l\rvert$	Photon velocity magnitude [m/s]	1×10^{-2}
Δt	Time step [s]	5×10^{-7}
c_p	Powder and substrate heat capacity [J/kg K]	481
ρ	Powder and substrate density [kg/m^3]	7990
δ_A	Substrate thickness [nm]	0.1

of mono-disperse spheres, denominated Random Loose Packing (RLP) in the literature [26], and falls within the range of powder bed densities used in LPBF [27]. It is consistent with the method of formation of the powder bed, i.e. sedimentation by means of gravity [28]. The powder bed is then struck with photons and the optical reflectivity of the particle and substrate material, R, is varied between 0 and 1 with a step of 0.1.

At $t = 0$, the photons are initialized on a plane at $z_l^0 = 0.5L_z$, with random and uniformly distributed horizontal coordinates $x_l^0 \in (0, L_x)$ and $y_l^0 \in (0, L_y)$. The photon velocity is initialized as $\mathbf{v}_l^0 = -|\mathbf{v}_l|\mathbf{e}_z$, while the polarization vector $\mathbf{z}_l^0$ lies in the $\mathbf{e}_x$-$\mathbf{e}_y$ plane. The simulation is advanced until all the photons leave the domain or exhaust their energy. Table 4 summarizes the simulation parameters.

The effective reflectivity R_{eff} is calculated from the total heat absorbed by the powder particles and the substrate, and the initial energy of the photons.

Fig. 7 shows the simulation results, with R_{eff} (black circles) as a function of the material optical reflectivity R. Between $R_{\text{eff}}(R = 0) = 0$ (total absorption) and $R_{\text{eff}}(R = 1) = 1$ (total reflection), highly absorptive materials ($R \lesssim 0.4$) exhibit essentially direct proportionality

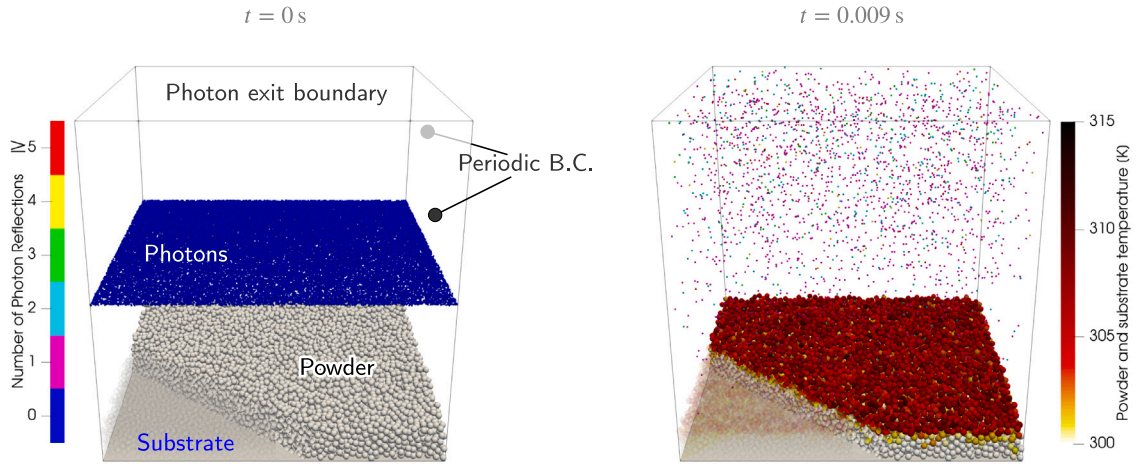

Fig. 6. Simulation set up of the powder bed, two successive snapshots. The powder particles and the substrate are colored by their temperature, the photon-type particles are colored by the number of reflection events $N_{r,l}$. Part of the powder particles are rendered in transparency, to show the underlying substrate. (For interpretation of the references to color in this figure legend, the reader is referred to the web version of this article.)

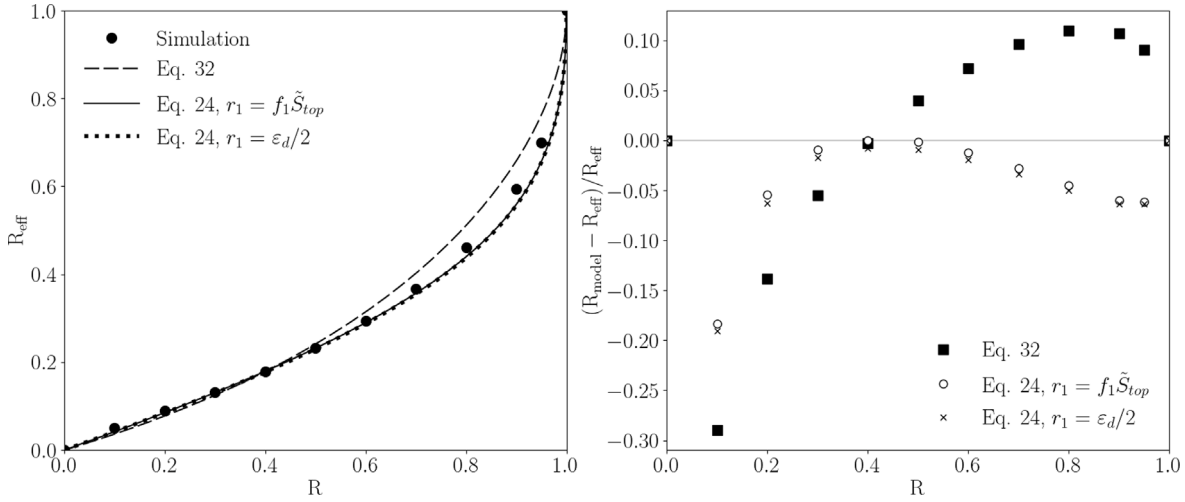

Fig. 7. Effective reflectivity of a thick powder bed versus optical reflectivity R: the left-side panel shows the simulation results (circles), compared with Eq. (32), Eq. (24) with $r_1 = f_1\tilde{S}_{top}$, and Eq. (24) with $r_1 = \varepsilon_d/2$ [29]. The right-side panel shows the relative error of the models over the R range.

between R_{eff} and R. For more reflective materials ($R \gtrsim 0.4$), the effects of multiple photon reflections become increasingly nonlinear, and R_{eff} approaches the total reflection limit ($R = 1$) with a growing steepness in the derivative (an additional simulation with $R = 0.95$ was added to show this more clearly).

As shown in Fig. 7, the results compare favorably to the correlation by Gusarov and Kruth [29,30]:

$$R_{\text{eff}} = r_1 R + (1 - r_1)\left(\frac{1 - \sqrt{1 - R}}{1 + 2\sqrt{1 - R}}\right), \tag{24}$$

where r_1 is the fraction of incident photons that are reflected only once, also called first reflection factor. The correlation is derived by modeling the powder bed as an equivalent absorbing and scattering medium of infinite thickness, characterized by three features: extinction coefficient, albedo, and scattering phase function. The radiative transfer equation (RTE) through the medium is approximated as a superposition of collimated and diffuse radiation flux components, which can be solved analytically. The effective reflectivity can then be obtained by the resulting energy flux, and by adding the energy directly back-reflected by the top layer of the powder (which does not penetrate the equivalent medium and is thus excluded from the energy flux components in the RTE) [30].

The factor r_1 can of course be calculated *a posteriori* from the simulation, but it is more interesting to estimate it *a priori* based on the morphology of the irradiated surface, thus enabling the use of Eq. (24) as a predictive tool for R_{eff}. The irradiated surface of a mono-disperse powder bed consists of a top layer of spherical particles, that receives most of the radiation transferred by the first reflection of the photons, as visible from the temperature distribution in the second snapshot of Fig. 6. It can be expected that the first reflection factor for vertical incident radiation, r_1, is proportional to the fractional horizontal projected area of the top layer, $r_1 = f_1\tilde{S}_{top}$, with the proportionality coefficient f_1 given by the fractional horizontal projected area of an individual sphere for which a vertically incident photon does not get caught by the nearest neighboring sphere after one reflection, but leaves the domain. Fig. 8(a) geometrically illustrates this occurrence in 2D, with neighboring circles: the photon l bounces off circle P_1, then grazes circle P_2 at a tangent, thus α_1 is the upper bound of the angle of incidence for which $N_{r,l} = 1$. For the 2D configuration $f_1 = \sin\alpha_1$; in 3D a reasonable estimation is to consider the spherical cap with polar angle α_1 (since in a randomly packed bed neighboring particles can be present in all directions with equal probability), whose horizontal projected area is $(\pi r_P^2 \sin^2\alpha_1)$, which gives $f_1 = \sin^2\alpha_1$. The angle α_1 can be calculated by generalizing for any distance Δ_P between neighboring

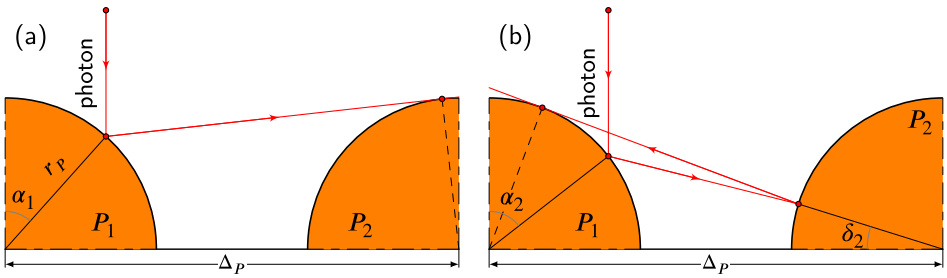

Fig. 8. Illustration of the angles of incidence for a pair of neighboring circles (P_1, P_2) with distance Δ_P between the two center points, irradiated by a photon perpendicular to the center points axis. In configuration (a), the photon l bounces off circle P_1, then grazes circle P_2 at a tangent, α_1 is the upper bound of the angle of incidence for which $N_{r,l} = 1$. In configuration (b), the photon l bounces off circle P_1, then gets reflected back by circle P_2, and finally grazes circle P_1 at a tangent, thus α_2 is the upper bound of the angle of incidence for which $N_{r,l} \leq 2$.

circles the procedure outlined in detail by Gusarov [29] (where the two neighboring circles touch each other: $\Delta_P = 2r_P$). The calculation gives:

$$f_1 = \sin^2 \alpha_1 = \left(\frac{1 + \sqrt{1 + 8\widetilde{\Delta}_P \left(\widetilde{\Delta}_P - 1 \right)}}{4\widetilde{\Delta}_P} \right)^2, \tag{25}$$

with $\widetilde{\Delta}_P = \Delta_P / r_P$. The top layer of powder particles for an irregular packing is not uniquely defined: in order to calculate $\tilde{S}_{top}$, an adequate outer shell for the whole collection of particles is given by the 3D alpha-shape with the alpha parameter equal to the particle diameter $2r_P$. A 3D alpha-shape is defined as the concave hull of a set of points S (in this case, the particle centers), that is obtained starting from the convex hull of S, and erasing all portions of the polytope that can be occupied by a sphere with radius alpha (or several such spheres), without any of the points of S being enclosed by the sphere [31]. The top layer of particles is then defined as the upper surface of the alpha-shape (Fig. 9), and $\tilde{S}_{top}$ as its fractional horizontal projected area. The average distance between neighboring particles in the top layer, Δ_P, is calculated with a nearest neighbors algorithm. Table 5 shows the values of $\tilde{S}_{top}$ and r_1 that result from the alpha-shape calculation applied to the powder bed.

Alternatively, Gusarov [29] suggests that r_1 can be obtained as half the fractional horizontal projected area of the top powder layer ($f_1 = 0.5$): in fact all vertical incident rays hitting a sphere within the spherical cap of polar angle $\alpha_1 = \pi/4$ (whose projected area is half the projected area of the sphere) will be back-reflected and leave the system. He then equates $\tilde{S}_{top}$ to the packing density ε_d, according to the principle of Delesse [32,33], so that $r_1 = \varepsilon_d/2$. Through the latter approximation, only the bulk properties of the powder bed (ε_d) are required to estimate r_1, eliminating the need for a far more complex measurement of surface properties. The value obtained in the present case is $r_1 = \varepsilon_d/2 = 0.287$, very close to 0.291 obtained from the top fractional projected area calculation, reported in Table 5. Therefore the plots of Eq. (24) with these two different values of r_1, shown in Fig. 7, only deviate very slightly from each other. It has to be noted, however, that the equivalence $\tilde{S}_{top} \approx \varepsilon_d$ is only satisfactory for homogeneous isotropic systems: the estimation of r_1 from ε_d fails for inhomogeneous and anisotropic bed arrangements, such as spheres packed in regular structures (see "Appendix B").

Eq. (24) condenses the influence of the surface morphology on R_{eff} into a single parameter, the first reflection factor r_1. An expression that also accounts for the second reflection factor r_2 can be derived in the following way. Let us first split R_{eff} into the sum of two terms, one accounting for the reflection by the horizontal projected area of the top powder layer, thus proportional to $\tilde{S}_{top}$, and the other accounting for the remaining exposed area. The former can be expressed as a power series of R, provided that the reflected energy is independent of the angle of incidence (this assumption will be discussed at the end of the Section); the latter by the reflectivity of the equivalent medium model by Gusarov and Kruth [30], since it represents the fraction of light that goes past the top powder layer and penetrates deeper into the bed:

$$R_{\text{eff}} = \tilde{S}_{top} \left(f_1 R + f_2 R^2 + \sum_{n=3}^{\infty} f_n R^n \right) + \left(1 - \tilde{S}_{top}\right) \left(\frac{1 - \sqrt{1-R}}{1 + 2\sqrt{1-R}} \right). \tag{26}$$

Here the coefficients f_n represent the fractional horizontal projected area of an individual sphere for which a vertically incident photon undergoes n reflections by the neighboring spheres before leaving the domain $\left(\sum_{n=1}^{\infty} f_n = 1\right)$. It is evident that the smaller the optical reflectivity R, the more Eq. (26) tends to be dominated by the first-order term, while the nonlinear terms become increasingly important when R approaches 1. The derivative of Eq. (26) is:

$$R'_{\text{eff}} = \tilde{S}_{top} \sum_{n=1}^{\infty} f_n n R^{n-1} + \frac{3\left(1 - \tilde{S}_{top}\right)}{2\sqrt{1-R}\left(1 + 2\sqrt{1-R}\right)^2}, \tag{27}$$

which increases and diverges to infinity as R approaches 1. These features are consistent with what is observed in Fig. 7, as already noted.

A closed expression for Eq. (26) can be found when the expressions for f_n are known. The first coefficient is given by Eq. (25). Similarly, the second coefficient f_2 is given by the fractional horizontal projected area of an individual sphere for which a vertically incident photon bounces onto the nearest neighboring sphere but does not get caught back after two reflections. Fig. 8(b) geometrically illustrates this occurrence in 2D: the photon l bounces off circle P_1, then off circle P_2 back towards circle P_1, which it grazes at a tangent, thus α_2 is the upper bound of the angle of incidence for which $N_{r,l} \leq 2$. In 3D a reasonable estimation for f_2 is to consider the difference of projected areas between the spherical cap with polar angle α_2 and the one with polar angle α_1, which gives:

$$f_2 = \sin^2 \alpha_2 - f_1. \tag{28}$$

The angle α_2 can be calculated by numerically solving for α_2 and δ_2 (see Fig. 8(b)) the following system:

$$\begin{cases} \left(\widetilde{\Delta}_P \cos 2\delta_2 - \cos \delta_2\right) \cos 2\alpha_2 + \left(2 \sin 2\delta_2 - \sin \delta_2\right) \sin 2\alpha_2 = 1; \\ \left(\widetilde{\Delta}_P - \sin \alpha_2 - \cos \delta_2\right) \cos 2\alpha_2 + \left(\cos \alpha_2 - \sin \delta_2\right) \sin 2\alpha_2 = 0, \end{cases} \tag{29}$$

which generalizes for any distance Δ_P between neighboring circles the procedure outlined in detail by Gusarov [29] (where the two neighboring circles touch each other: $\Delta_P = 2r_P$).

The subsequent reflection coefficients are expressed by:

$$f_n = \sin^2 \alpha_n - \sin^2 \alpha_{n-1} = \sin^2 \alpha_n - \sum_{j=1}^{n-1} f_j. \tag{30}$$

Gusarov [29] has numerically calculated the first 12 reflection coefficients in 2D through ray tracing, hence the first 12 angles α_n when $\Delta_P = 2r_P$. A reasonable approximation for $\sin^2 \alpha_n$ with $n > 2$ is (Fig. 10):

$$\sin^2 \alpha_n = 1 - \frac{2}{n}\left(1 - f_1 - f_2\right). \tag{31}$$

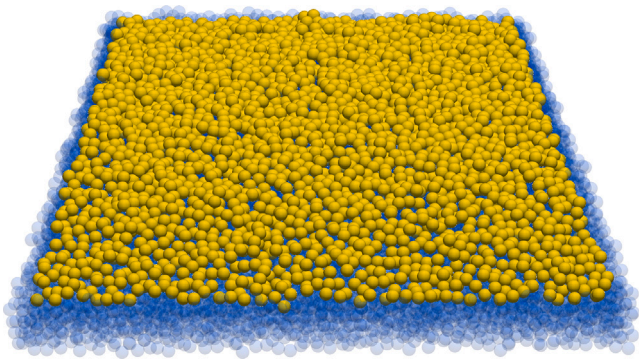

Fig. 9. Particles that form the top layer of the powder bed (in yellow) are picked as the upper boundary of the 3D alpha-shape obtained by setting alpha = $2r_P$. (For interpretation of the references to color in this figure legend, the reader is referred to the web version of this article.)

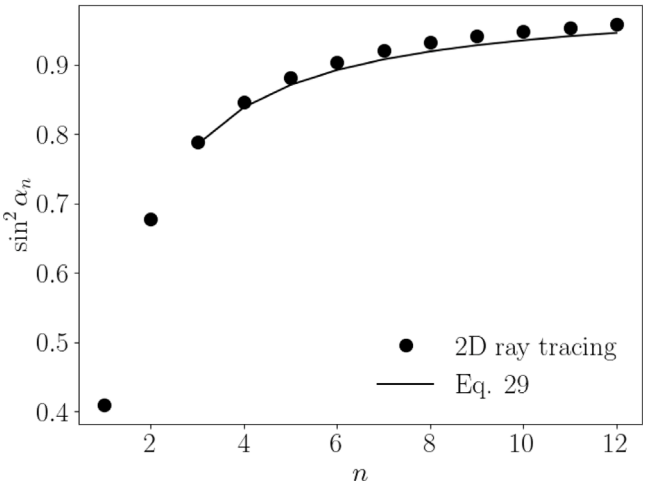

Fig. 10. Squared sine of the angle of incidence for the first 12 reflections in a 2D row of circles.
Source: Ray tracing data from Gusarov [29].

Table 5
Geometric factors for the top layer of particles of the powder bed.

$\tilde{S}_{top}$	0.708
r_1	0.291
r_2	0.189

Using Eqs. (31) and (30), a closed expression for the infinite series in Eq. (26) can be found, thus obtaining:

$$R_{\text{eff}} = \tilde{S}_{top}\left\{f_1 R + f_2 R^2 + \left(1 - f_1 - f_2\right)\left[R\left(2 - R\right) + 2\left(1 - R\right)\ln\left(1 - R\right)\right]\right\} + \left(1 - \tilde{S}_{top}\right)\left(\frac{1 - \sqrt{1 - R}}{1 + 2\sqrt{1 - R}}\right). \tag{32}$$

Eq. (32) is compared to Eq. (24) and compared to the simulation data in Fig. 7. For $R \lesssim 0.5$, the two correlations are very close, predicting similar values of R_{eff}. However, as the optical reflectivity increases, Eq. (32) tends to overpredict the effective reflectivity. This can be explained by the fact that the power series expansion used to derive Eq. (32) neglects the effect of the angle of incidence on the energy transfer, and it has already been shown in Fig. 5 that polarization effects increase the absorptivity for a wide range of angles of incidence, with the effect becoming very large for large values of R.

Thus, we conclude that for thick powder beds it is sufficient to estimate the first reflection factor r_1 to get a good estimate of the bed effective reflectivity. However, in the following section, we show that this is not the case for sparse powder layers, for which the inclusion of the second reflection factor is necessary to obtain a satisfactory prediction.

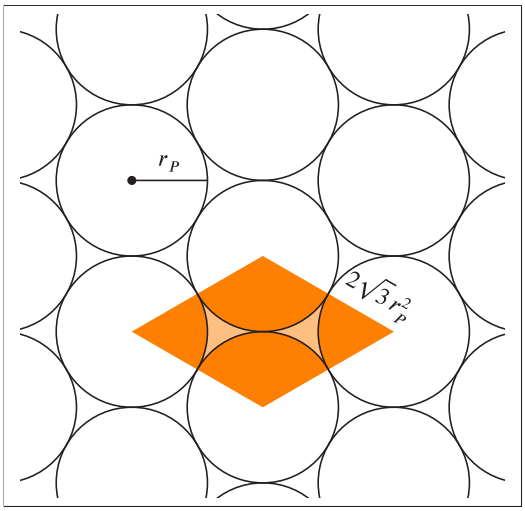

Fig. 11. 2D layer of equal spheres arranged into a regular hexagonal lattice, view from the top. The highlighted area measures $2\sqrt{3}r_P^2$ and is the unit area cell the contains one sphere.

A correlation for the absorption of a laser beam by a sparse layer of powder particles

Sometimes it is desirable to know the absorption properties of thin powder beds, or sparse layers of powder particles distributed over a substrate (formed, for instance, by spilling/spattering of powder particles from a nearby powder bed or by condensation, redeposition, and solidification of vapors). Certain rough surfaces with low waviness (i.e. with an approximately flat mean surface) can also be usefully modeled as a sparse layer of particles over a flat substrate, with the particle diameter taken as the characteristic size of the roughness elements, and the layer density inversely related to the spatial autocorrelation length scale of the roughness elements.

The sparseness/thickness of a layer with N_P particles can be characterized by a parameter Ψ, which represents the number of stacked 2D layers of spheres arranged in a regular hexagonal lattice (see Fig. 11) over a flat substrate with area S_{sub}:

$$\Psi = \frac{N_P}{S_{sub}/\left(2\sqrt{3}r_P^2\right)}. \tag{33}$$

For $\Psi \leq 1$, the substrate is only partially covered by powder particles: the fractional surface that back-reflects vertical incident light one time includes the horizontal projected area of the particles, $\tilde{S}_{top} = \frac{N_P \pi r_P^2}{S_{sub}} = \frac{\pi}{2\sqrt{3}}\Psi$, as well as the uncovered portion of the substrate, so that the first reflection factor can be expressed as:

$$r_1 = f_1 \frac{\pi}{2\sqrt{3}}\Psi + \left(1 - \frac{\pi}{2\sqrt{3}}\Psi\right). \tag{34}$$

The second reflection factor only involves the horizontal projected area of the particles:

$$r_2 = f_2 \frac{\pi}{2\sqrt{3}}\Psi. \tag{35}$$

The coefficients f_1 and f_2 in Eqs. (34) and (35) are calculated from Eqs. (25) and (28), where the normalized average distance between

particles, $\widetilde{\Delta}_P$, can be estimated pretending that the powder layer is arranged in a regular hexagonal lattice, so that:

$$\widetilde{\Delta}_P = \frac{2}{\sqrt{\Psi}}. \tag{36}$$

Using these Ψ-dependent values of r_1 and r_2, a correlation for the effective reflectivity of the sparse powder layer ($\Psi \leq 1$) can be derived in a similar fashion to Eq. (32), obtaining:

$$R_{\text{eff}} = r_1 R + r_2 R^2 + \left(1 - r_1 - r_2\right)\left[R\,(2 - R) + 2\,(1 - R)\ln\,(1 - R)\right]. \tag{37}$$

To evaluate the predictive capability of Eq. (37), and how it compares with Eq. (24) as the thickness of the powder layer increases, we simulated the laser absorption by a sparse layer of particles using the same configuration as in Section "Laser absorption on a thick powder bed", and varying the number of particles N_P dropped on the substrate. Six configurations with increasing Ψ were investigated, shown in Fig. 12; one can distinguish between sparse powder layers when $\Psi < 1$ and proper powder beds when $\Psi > 1$. The last configuration ($\Psi = 4.962$) corresponds to the thick powder bed of Section "Laser absorption on a thick powder bed". Four values of the optical reflectivity of the material, R, were tested.

Fig. 13 shows the effective reflectivity data from the simulations (circles) versus the sparseness/thickness parameter Ψ. For $\Psi \leq 1$, the data are compared with Eq. (37) (dashed lines) and Eq. (24) (solid lines), where r_1 is calculated using Eq. (34). As expected, in this sparseness range, Eq. (37) is superior, giving a more accurate prediction for R_{eff} and for its slope as Ψ varies from 0 to 1, especially for large values of optical reflectivity R. For $1 < \Psi \leq 2$ the powder layer is neither sparse nor thick; in this region, the simulation data point is compared to the predictions of Eq. (32) (dashed lines) and Eq. (24) (solid lines), with the values of r_1 and r_2 taken from Table 5. In this intermediate region, the correlation that accounts for both r_1 and r_2 (Eq. (32)) still overall outperforms the single-parameter Eq. (24). For $\Psi > 2$, the effective reflectivity asymptotically approaches that of a thick powder bed, which can be predicted by Eq. (24) with better accuracy, as already shown in Section "Laser absorption on a thick powder bed" and Fig. 7. Fig. 13 also shows the relative error of the correlation predicted values compared to the simulation data points.

In a real-life scenario, the sparseness parameter Ψ cannot be calculated directly as in Eq. (33). However, an equivalent value of Ψ can be determined for a sparse powder layer, provided that a realistic estimate $\tilde{S}^*_{top}$ for fractional surface coverage is available:

$$\Psi_{eq} = \frac{2\sqrt{3}\tilde{S}^*_{top}}{\pi}. \tag{38}$$

The value of $\tilde{S}^*_{top}$ can be estimated, for instance, by image processing of SEM snapshots of the powder layer, as we have demonstrated in a separate publication [20]. In the same publication, we have used Eq. (37) to predict the effective laser absorptivity of copper surfaces covered by powder layers formed by vapor condensation and redeposition, thus validating the correlation and providing an example of its practical use.

Conclusions

A novel numerical model for the simulation of laser absorption on rough solid surfaces is presented, described, and applied to two scenarios representative of applications. The numerical framework is based on the DEM software Aspherix®; the laser beam is modeled as a collection of massless, frictionless photon-type DEM particles, adapting the Aspherix® DEM algorithm to include photon interaction laws for specular reflection, energy transfer, and light polarization. The photon-type particles benefit from the same efficient parallelization as the standard-type DEM particles, making the numerical framework suitable for high-performance computing. The implementation of photon-type particle interaction laws is not limited to reflection on boundaries and mesh elements, but includes reflection on standard-type DEM particles: thus a variety of configurations involving both meshed geometry and material particles at the same time can be studied.

The numerical model is applied to a stereophotogrammetry reconstruction of a rough copper plate, demonstrating the accuracy of the model and the importance of the inclusion of polarization-dependent reflectivity in the framework, according to the Fresnel reflection law. We demonstrate that ignoring the evolution of the light rays polarization leads to significant overprediction of the effective reflectivity for a rough surface, and can only be considered an acceptable approximation when the optical reflectivity of the material is very low. In fact, the inverse procedure of determining the roughness of a surface by measuring the polarization characteristics of the reflected light is an already established technique in the literature [34]. A quantitative assessment of the polarization-invariant model error is left to future investigation, as it would require an accurate experimental characterization of the rough surface hemispherical reflectance, which is beyond the scope of the present work.

As powder beds are one of the most common occurrences of rough surfaces in laser applications, we show the capability of the numerical model to treat laser reflections on material particles by simulating the absorption on a bed of monodisperse spheres. The simulation results agree well with the algebraic model for the powder bed reflectivity found in the literature [29].

Stemming from the analysis of this algebraic model and from the powder-bed simulations, we propose a new correlation for the effective reflectivity of sparse powder layers, that parameterizes the properties of the reflecting surface with the powder-layer sparseness, capturing the change in effective reflectivity as the layer gets denser. Compared with simulation data, we show that the new correlation provides a better prediction of the effective reflectivity of sparse to intermediate powder layers than the model for thicker powder beds available in the literature.

Future work will focus on further development of the numerical model, to integrate the laser method with dynamic geometry and moving particles, with the goal of simulating Directed Energy Deposition (DED), a laser additive manufacturing process controlled by the interaction of the laser beam with a high-speed stream of material particles, whose complexity has so far hindered the feasibility of a complete numerical model. The first steps in this direction have been recently published, demonstrating the robustness of our framework and its complementarity to experimental observations with high-speed visible and spectral cameras [35]. In addition, the modeling effort will be extended to polydisperse powder beds and layers.

CRediT authorship contribution statement

Giandomenico Lupo: Writing – review & editing, Writing – original draft, Visualization, Investigation, Formal analysis, Data curation. **Martin Niemann:** Writing – review & editing, Software. **Christoph Goniva:** Writing – review & editing, Software. **Wojciech Szmyt:** Writing – review & editing, Visualization, Validation. **Xiao Jia:** Writing – review & editing, Validation. **Vladyslav Turlo:** Writing – review & editing, Supervision, Resources, Project administration, Funding acquisition, Conceptualization.

Declaration of competing interest

The authors declare that they have no known competing financial interests or personal relationships that could have appeared to influence the work reported in this paper.

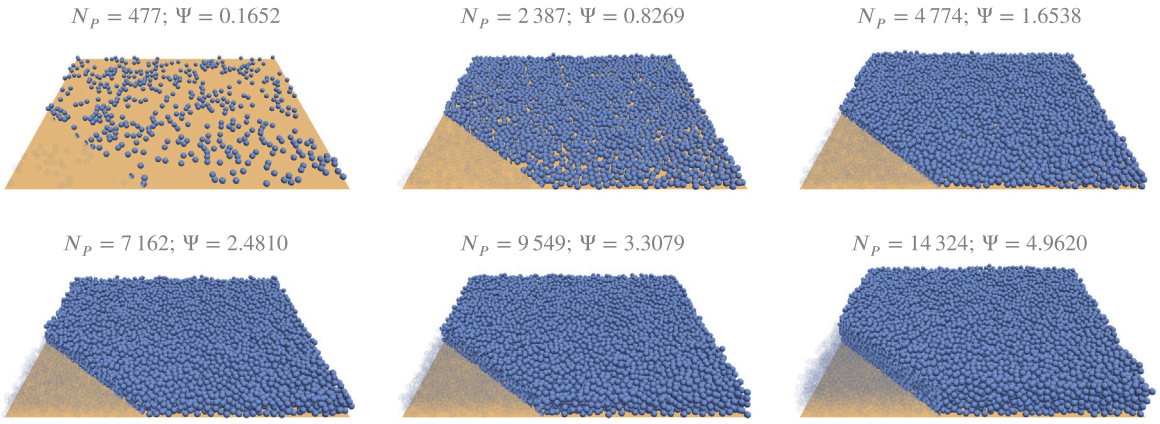

Fig. 12. Sparse layer of spherical powder particles, that becomes a progressively thicker powder bed, as N_P and Ψ are increased. Some of the powder particles are rendered in transparency, to show the underlying substrate.

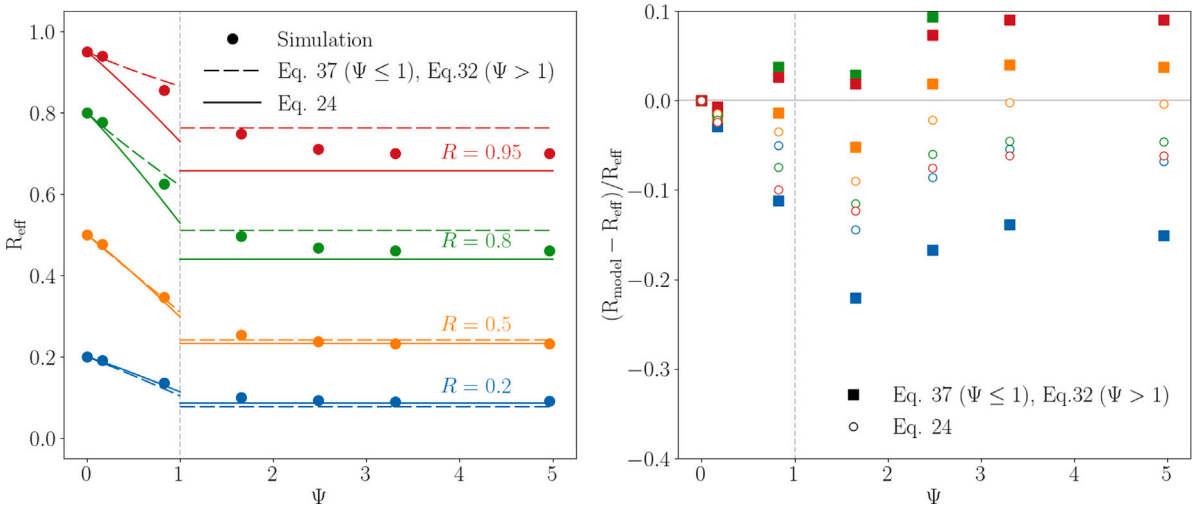

Fig. 13. Effective reflectivity of different powder layers versus the sparseness/thickness parameter Ψ, for four values of the optical reflectivity R: the left-side panel shows the simulation results (circles), compared with Eqs. (37)/(32) and Eq. (24); the right-side panel shows the relative error of the models. The two regions of sparse powder layers ($\Psi \leq 1$), and powder beds ($\Psi > 1$) are distinguished. For $\Psi = 0$, only the substrate is present and the value of R_{eff} is equal to the optical reflectivity, as all vertical light is reflected once ($r_1 = 1$).

Acknowledgments

We thank the Bern Economic Development Agency, Switzerland for financial support and the Swiss National Supercomputing Centre for computing time (the s1130 project). We thank Prof. Patrik Hoffmann and Dr. Akash Aggarwal for fruitful discussions.

Appendix A

The reflectivity at normal incidence of the rough copper plate used to generate the meshed geometry of Section "Laser absorption on a rough metallic surface" was measured with the same apparatus used to characterize the polished sample [20], and is reported in Table A.1. The error of $\widetilde{R}$ is propagated as the sum of the relative errors of numerator and denominator in Eq. (23). The surface roughness on the sample was generated during a microwelding experiment, by the re-deposition of nanoparticles formed by the condensation of metal and oxide vapors [20]. The reflectivity measurement was performed at a point on the sample at a distance of (18.3 ± 2.5) μm from the welding track, which corresponds to the center of the patch that was afterwards scanned with an electron microscope and converted into topography data to generate the meshed geometry.

Table A.1
$\widetilde{R}$ of the copper sample.

Experiment	$\left(54.2^{+3.3}_{-2.9}\right)\%$
Simulation (Fresnel)	54.4%

The measurement of Table A.1 represents a lower bound for the effective reflectivity of the rough sample, as the design of the measurement apparatus does not guarantee that the entirety of the diffuse reflection caused by the roughness elements is captured (an integrating sphere would be necessary for that). Therefore the measurement cannot be used to support a quantitative validation of the numerical method, and it is thus reported in this appendix.

Appendix B

The first reflection factor r_1 is estimated according to $r_1 = f_1 \tilde{S}_{top}$, for 12 regular packings of equal spheres. Each packing is obtained as a rotation of one of four regular lattices, diamond (DI), simple cubic (SC), body-centered cubic (BCC), and face-centered cubic (FCC), aligned with one of three planes, with Miller indices (100), (110) and (111) respectively. The first reflection coefficient f_1 is calculated

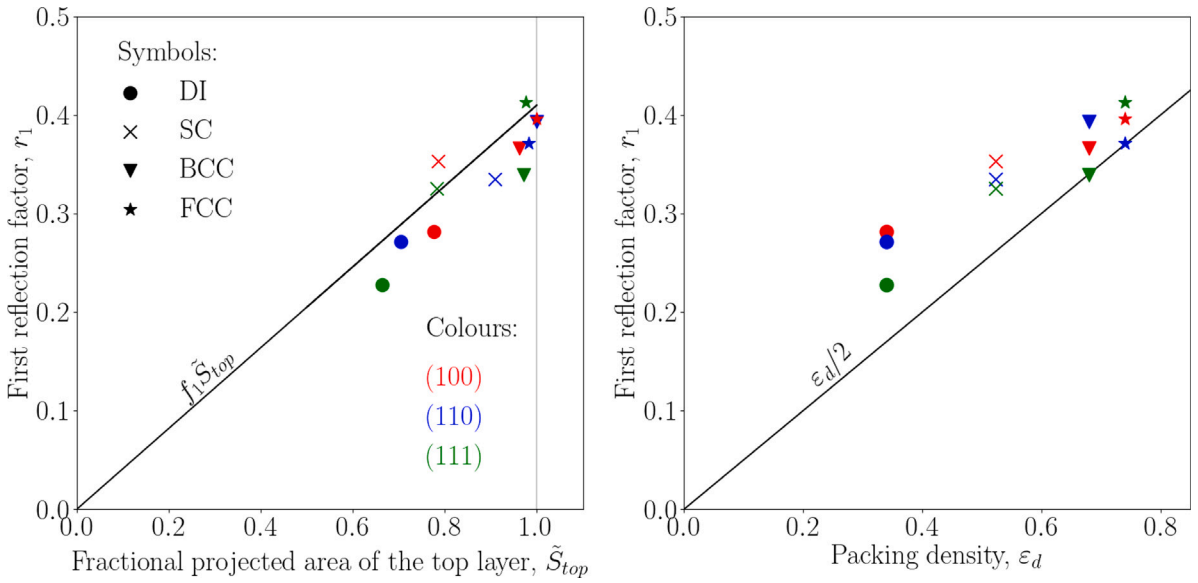

Fig. B.1. First reflection factor for regular packings of equal spheres. Comparison of the 3D ray tracing data from Gusarov [29] with $r_1 = f_1\tilde{S}_{top}$ (left panel) and $r_1 = \varepsilon_d/2$ (right panel).

Table B.1
Fractional horizontal projected area of the top layer for regular packings of equal spheres.

Packing		$\tilde{S}_{top}$
DI	(100)	$\frac{9}{32}\pi - \frac{3}{4}\cos^{-1}\left(\sqrt{\frac{2}{3}}\right) + \frac{1}{2\sqrt{2}}$
DI	(110)	$\frac{3}{8\sqrt{2}}\pi - \frac{3}{8\sqrt{2}}\cos^{-1}\left(\frac{1}{\sqrt{3}}\right) + \frac{1}{8}$
DI	(111)	$\frac{3}{8\sqrt{3}}\pi - \frac{27}{8\sqrt{3}}\cos^{-1}\left(\frac{2\sqrt{2}}{3}\right) + \frac{1}{4}\sqrt{\frac{2}{3}}$
SC	(100)	$\frac{\pi}{4}$
SC	(110)	$\frac{\pi}{4\sqrt{2}} + \frac{1}{2\sqrt{2}}$
SC	(111)	$\frac{\sqrt{3}}{6}\pi - \frac{\sqrt{3}}{2}\cos^{-1}\left(\sqrt{\frac{2}{3}}\right) + \frac{\sqrt{6}}{6}$
BCC	(100)	$\frac{3}{8}\pi - \frac{3}{2}\cos^{-1}\left(\sqrt{\frac{2}{3}}\right) + \frac{1}{\sqrt{2}}$
BCC	(110)	1
BCC	(111)	$\frac{3\sqrt{3}}{16}\pi - \frac{9\sqrt{3}}{8}\cos^{-1}\left(\frac{2\sqrt{2}}{3}\right) + \frac{3}{4}\sqrt{\frac{2}{3}}$
FCC	(100)	1
FCC	(110)	$\frac{\sqrt{2}}{12}\pi + \frac{\sqrt{6}}{4}$
FCC	(111)	$\frac{\sqrt{3}}{3}\pi - \sqrt{3}\cos^{-1}\left(\frac{\sqrt{3}}{3}\right) + \frac{\sqrt{6}}{3}$

from Eq. (25); the fractional projected area of the top layer $\tilde{S}_{top}$ is calculated by selecting the top spheres of the alpha-shape concave hull as described in Section "Laser absorption on a thick powder bed" (Table B.1).

Fig. B.1 compares the values of r_1 obtained as $f_1\tilde{S}_{top}$ and $\varepsilon_d/2$ to the 3D ray tracing calculations by Gusarov [29]. The estimation via the packing density ε_d leads to consistent underprediction of r_1, with an average relative error of 17.3% and a maximum relative error of 39.6% for DI (100). It is clear that equating volume fraction and area fraction (principle of Delesse) for anisotropic packing structures only works when the area fraction is the average of all possible 2D sections of the 3D unit cell [33], and not with the area fraction of one particular orientation. The estimation via the fractional horizontal projected area of the top layer is much closer to the actual ray tracing data for r_1, with an average error of 8.7% and a maximum error of 19.5% for DI (111).

Appendix C. Supplementary data

Supplementary material related to this article can be found online at https://doi.org/10.1016/j.rinp.2024.108043.

Data availability

Data will be made available on request.

References

[1] Cook PS, Murphy AB. Simulation of melt pool behaviour during additive manufacturing: Underlying physics and progress. Addit Manuf 2020;31:100909.
[2] Tolochko N, Khlopkov Y, Mozzharov S, Ignatiev M, Laoui T, Titov V. Absorptance of powder materials suitable for laser sintering. Rapid Prototyp J 2000;6(3):155–61.
[3] King WE, Anderson AT, Ferencz RM, Hodge NE, Kamath C, Khairallah SA, Rubenchik AM. Laser powder bed fusion additive manufacturing of metals; physics, computational, and materials challenges. Appl Phys Rev 2015;2(4):041304.
[4] Boley CD, Khairallah SA, Rubenchik AM. Calculation of laser absorption by metal powders in additive manufacturing. Appl Opt 2015;54(9):2477–82.
[5] Sun Y. Statistical ray method for deriving reflection models of rough surfaces. J Opt Soc Amer A 2007;24(3):724–44.
[6] Beckmann P, Spizzichino A. The scattering of electromagnetic waves from rough surfaces. Pergamon Press; 1963.
[7] Voti RL, Leahu GL, Gaetani S, Sibilia C, Violante V, Castagna E, Bertolotti M. Light scattering from a rough metal surface: theory and experiment. J Opt Soc Am B 2009;26(8):1585–93.
[8] Xu GX, Wu CS, Qin GL, Wang XY, Lin SY. Adaptive volumetric heat source models for laser beam and laser + pulsed GMAW hybrid welding processes. Int J Adv Manuf Technol 2011;57:245–55.
[9] Wang XC, Kruth JP. A simulation model for direct selective laser sintering of metal powders, in computational techniques for materials, composites and composite structures. In: Computational techniques for materials, composites and composite structures. Civil-Comp Press; 2000, p. 57–71.
[10] Zhu Q, Zhao Z, Yan J. Multi-physics modeling of the 2022 NIST additive manufacturing benchmark (AM-bench) test series. Comput Mech 2024;1–18.
[11] https://www.aspherix-dem.com/.
[12] Flint TF, Robson JD, Parivendhan G, Cardiff P. Laserbeamfoam: Laser ray-tracing and thermally induced state transition simulation toolkit. SoftwareX 2023;21:101299.
[13] Ren Z, Zhang DZ, Fu G, Jiang J, Zhao M. High-fidelity modelling of selective laser melting copper alloy: Laser reflection behavior and thermal-fluid dynamics. Mater Des 2021;207:109857.
[14] Cheng H, Lee YC. Quantum theory of photon interaction in a plasma. Phys Rev 1966;142:104–14.
[15] Hecht E. Optics. Addison-Wesley; 2002.
[16] Schlick C. An inexpensive BRDF model for physically-based rendering. Comput Graph Forum 1994;13(3):233–46.
[17] Johnson E, Hicdurmaz S, Buck R, Hoffschmidt B. Beam radiation penetration in particle beds for heat transfer modeling of a centrifugal solar particle receiver. J Quant Spectrosc Radiat Transfer 2023;295:108403.

[18] Paivasaari K, Kaakkunen JJJ, Kuittinen M, Jaaskelainen T. Enhanced optical absorptance of metals using interferometric femtosecond ablation. Opt Express 2007;15(21):13838–43.
[19] Shanks K, Senthilarasu S, Mallick TK. Optics for concentrating photovoltaics: Trends, limits and opportunities for materials and design. Renew Sustain Energy Rev 2016;60:394–407.
[20] Jia X, Lupo G, Leparoux M, Turlo V, Hofmann P. Energy-effcient microwelding of copper by continuous-wave green laser: insights into nanoparticle-assisted absorptivity enhancement. Appl Surf Sci 2024;675:160940.
[21] Zediker MS, Fritz RD, Finuf MJ, Pelaprat JM. Laser welding components for electric vehicles with a high-power blue laser system. J Laser Appl 2020;32(2):022038.
[22] Haubold M, Ganser A, Eder T, Zäh MF. Laser welding of copper using a high power disc laser at green wavelength. Procedia CIRP 2018;74:446–9.
[23] Mohanta A, Leistner M, Leparoux M. Influence of temporal and spectral profiles of lasers on weld quality of titanium. Opt Lasers Eng 2020;134:106173.
[24] https://www.digitalsurf.com/software-solutions/multi-instrument/.
[25] Cignoni P, Callieri M, Corsini M, Dellepiane M, Ganovelli F, Ranzuglia G. MeshLab: an Open-Source Mesh Processing Tool. In: Scarano V, Chiara RD, Erra U, editors. Eurographics Italian chapter conference. The Eurographics Association; 2008.
[26] Onoda GY, Liniger EG. Random loose packings of uniform spheres and the dilatancy onset. Phys Rev Lett 1990;64:2727–30.
[27] Li Z, Mizutani M. Influence of layer thickness and substrate bed on the void fraction of powder layers for laser powder bed fusion. Powder Technol 2023;418:118293.
[28] Haughey DP, Beveridge GSG. Structural properties of packed beds — A review. Can J Chem Eng 1969;47(2):130–40.
[29] Gusarov AV. Radiative transfer, absorption, and reflection by metal powder beds in laser powder-bed processing. J Quant Spectrosc Radiat Transfer 2020;257:107366.
[30] Gusarov AV, Kruth JP. Modelling of radiation transfer in metallic powders at laser treatment. Int J Heat Mass Transfer 2005;48(16):3423–34.
[31] Edelsbrunner H, Mücke EP. Three-dimensional alpha shapes. ACM Trans Graph 1994;13(1):43–72.
[32] Delesse A. Procédé mécanique pour déterminer la composition des roches. Paris: F. Savy Édituer; 1866.
[33] Underwood EE. Stereology, or the quantitative evaluation of microstructures. J Microsc 1969;89(2):161–80.
[34] Das T, Bhattacharya K. Topometry of metal surfaces using reflection of polarized light. Optik 2021;243:167448.
[35] Aggarwal A, Pandiyan V, Leinenbach C, Leparoux M. Investigating laser beam shadowing and powder particle dynamics in directed energy deposition through high-fidelity modelling and high-speed imaging. Addit Manuf 2024;91:104344.